*Cell*, Volume *132*

# Supplemental Data

# Structure of the Dual Enzyme Ire1 Reveals the Basis for Catalysis and Regulation in Nonconventional RNA Splicing

**Kenneth P. K. Lee, Madhusudan Dey, Dante Neculai, Chune Cao, Thomas E. Dever, and Frank Sicheri**

**Table S1. Data collection and refinement statistics**

| | phospho-Ire1-ADP crystal |
|---|---|
| Data collection | |
| Space group | P6(5) |
| cell dimensions | |
| a,b,c (Å) | 130.30,130.30,175.01 |
| Resolution (Å) | 2.4 |
| $R_{sym}$ (%) | 6.02 |
| I/σI | 27.75 (5.02) |
| Completeness (%) | 99.9 (99.9) |
| Redundancy | 43.4 |
| | |
| Refinement | |
| Resolution (Å) | 2.4 |
| No. reflections | 65619 |
| $R_{work}/R_{free}$ (%) | 23.8/27.2 (26.7/34.7) |
| No. atoms | |
| protein | 65055 |
| ligand/ion | 56 |
| R.m.s. deviations | |
| Bond lengths (Å) | 0.014 |
| Bond angles (Å) | 1.7024 |
| Ramachandran data | |
| Most favored | 89.4% |
| Additionally allowed | 10.6% |
| Generously allowed | 0.0% |
| Disallowed | 0.0% |

Bracketed terms correspond to highest resolution shell (2.49 to 2.4Å)

$R_{sym} = 100 \times \Sigma|I - I>|/\Sigma<I>$, where I is the observed intensity and <I> is the average intensity from multiple observations of symmetry-related reflections.

$R_{free}$ was calculated with 10% of the data.

Supplementary Figure 1

A Wild type vs. kinase dead mutant

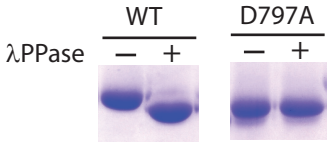


B Autophosphorylation of Ire1$^{cyto}$ occurs in *trans*

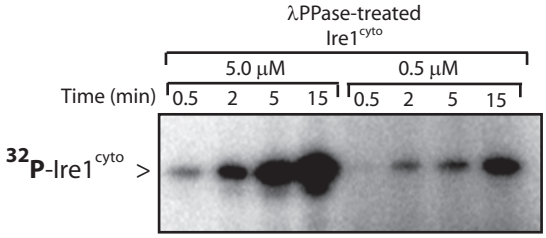


C Mass spectrometry identified four sites of phosphorylation in the activation segment of Ire1

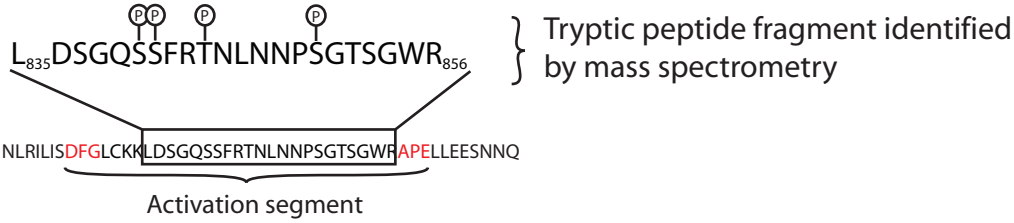


D Characterization of sites of autophosphorylation in activation segment of Ire1 in yeast

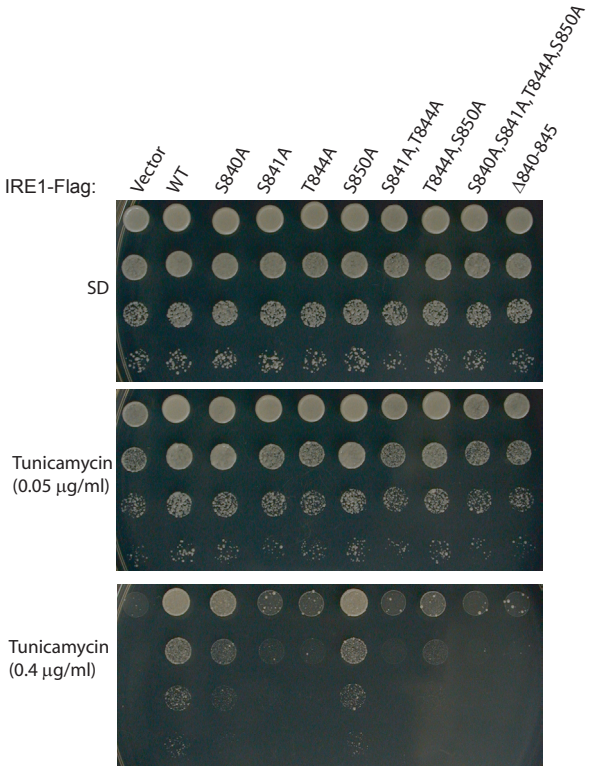

**Figure S1.** Phosphorylation status of Ire1$^{cyto}$ and analysis of activation segment autophosphorylation.
**(A)** Lambda phage phosphatase (λPPase) treatment of wild-type Ire1$^{cyto}$ purified from bacteria results in a quantitative mobility shift of the protein on SDS-PAGE consistent with the presence of stociometric phosphorylation on Ire1$^{cyto}$. In contrast, the protein kinase deficient mutant Ire1$^{cyto(D797A)}$ purified from bacteria is unaffected by λPPase treatment.
**(B)** Autophosphorylation of λPPase treated Ire1$^{cyto}$ occurs in *trans*. Kinase reactions in the presence of $^{32}$P-[γ]-ATP were performed using equivalent quantities but different concentrations of dephosphorylated wild-type Ire1$^{cyto}$. Identical amounts of protein were sampled from the reactions at different time points and analyzed by SDS-PAGE. The degree of $^{32}$P incorporation was assessed by autoradiography. The phosphorylated species is indicated with an arrow. The observed concentration dependence of autophosphorylation efficiency is consistent with autophosphorylation occurring in *trans*.
**(C)** Mass spectrometry analysis of tryptic peptide fragments reveals four stoichiometrically phosphorylated sites within the activation segment of Ire1$^{cyto}$. Phosphorylated positions correspond to S840, S841, T844, and S850. The tryptic peptides were analyzed by liquid chromatography mass spectrometry utilizing an ABI/Sciex Tempo 1Dplus LC (Applied Biosystems, Foster City, CA) into an ABI/Sciex QSTAR Elite mass spectrometer (ABI/Sciex, Foster City, CA).
**(D)** Characterization of autophosphorylation sites within the activation segment of yeast Ire1. Full-length yeast Ire1 constructs containing the indicated mutations in the activation segment were transformed in to an *ire1-null* yeast strain and assayed for rescue of growth in the presence of different concentrations of tunicamycin. Mutation of the newly identified sites T844 but not S850 impaired Ire1 function in vivo to a similar (or greater) extent as the previously identified sites S841 and S840. The Δ840-845 mutation corresponds to 6 residue deletion within the activation segment.

Supplementary Figure 2

A Kinase domain dimerization interface (Interface 1) mutants

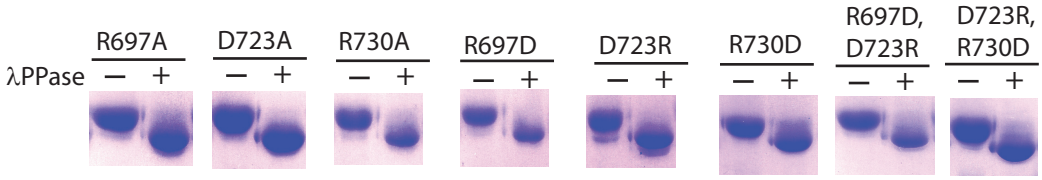


B KEN domain dimerization interface mutants

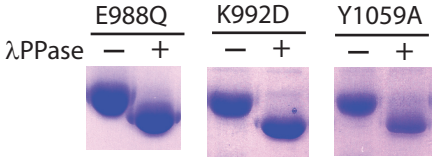


C Nuclease active site mutants

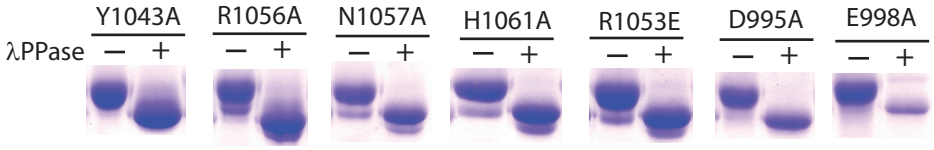


D Nuclease active site disordered loop mutants

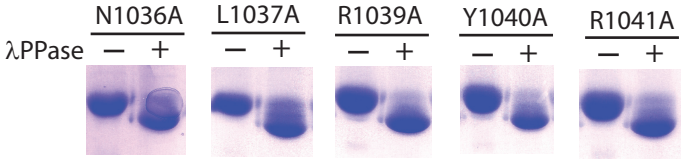


E Kinetics of KEN domain dimerization interface and nuclease active site mutants autophosphorylation

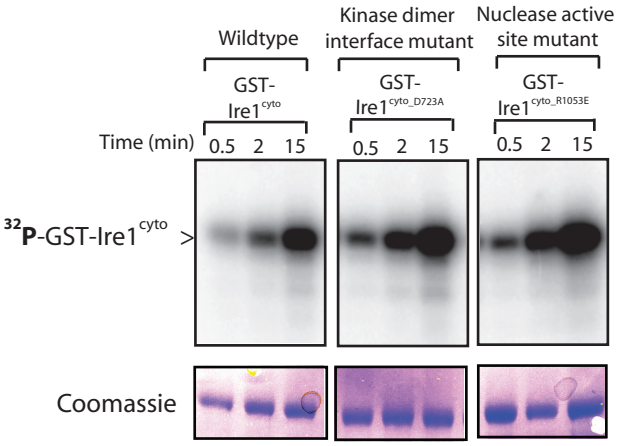

**Figure S2.** Phosphorylation status of Ire1$^{cyto}$ mutants and analysis of the impact of key mutations on Ire1$^{cyto}$ protein kinase activity.
**(A),(B),(C),&(D)** λPPase treatment of the indicated Ire1$^{cyto}$ mutants purified from bacteria as performed for the wild-type protein in **Supplementary Figure 1A**. A quantitative mobility shift of the protein on SDS-PAGE indicated competence for protein kinase phosphotransfer activity.
**(E)** Mutation of key nuclease inactivating residues in the kinase domain dimer interface or the nuclease active site in the KEN domain does not affect the ability of Ire1$^{cyto}$ to autophosphorylate. Kinase assays of lambda phosphatase treated GST-fusions of Ire1$^{cyto}$ mutants in the presence of $^{32}$P-[γ]-ATP were performed as for non-tagged wild-type Ire1$^{cyto}$ in **Supplementary Figure 1B**.

Supplementary Figure 3

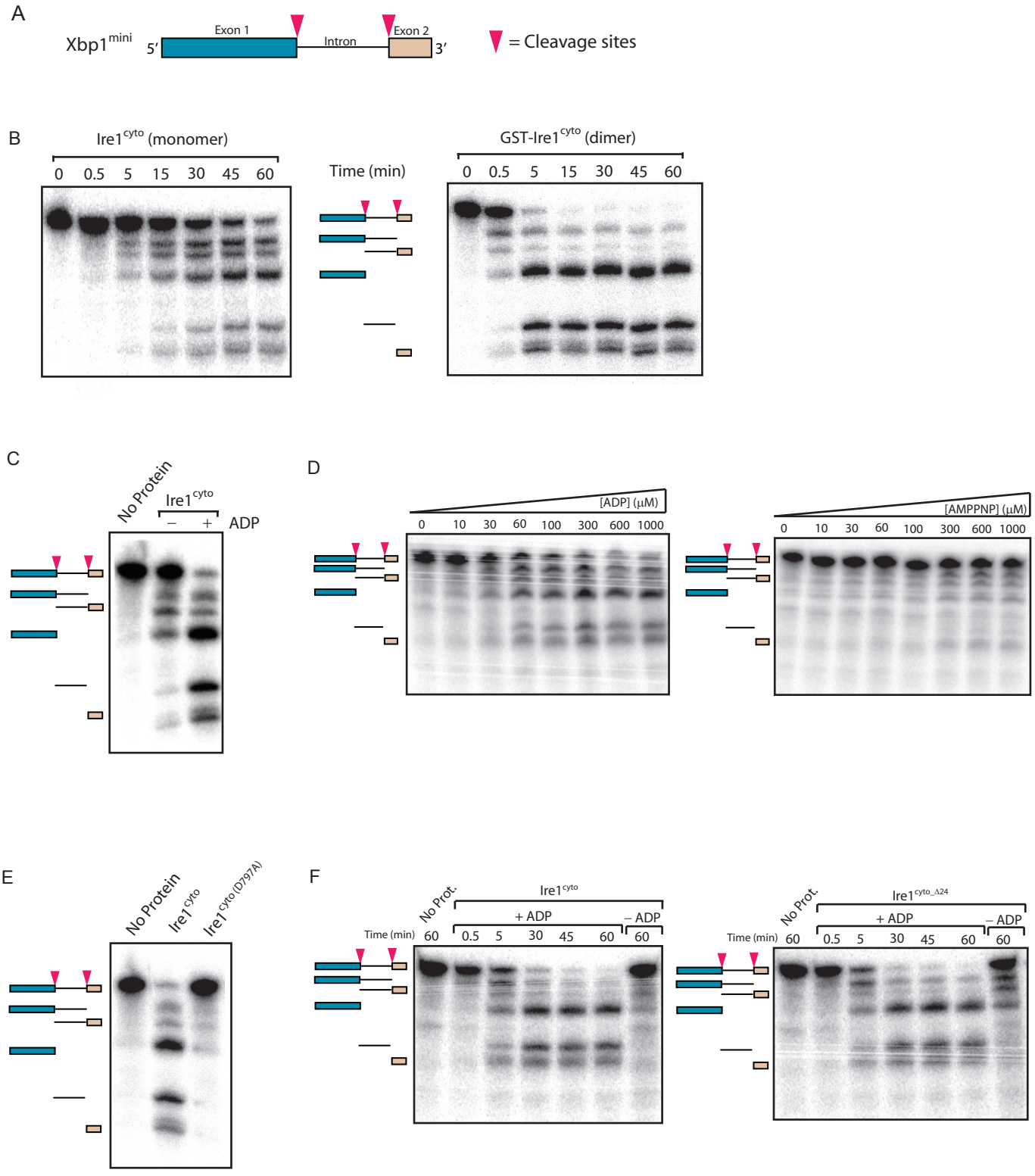

**Figure S3.** Ire1$^{cyto}$ displays known properties of full-length Ire1
**(A)** Schematic of the model tandem RNA hairpin substrate Xbp1$^{mini}$ used in this study. Exons are indicated by colored boxes, while the intron excised by Ire1 is indicated by a thin black line. Cleavage sites in the 5' and 3' hairpins are indicated by pink triangles. Secondary structure of the RNA is omitted for clarity.
**(B)** Enforced dimerization of Ire1$^{cyto}$ enhances kinetics of ribonuclease cleavage. Radiolabelled Xbp1$^{mini}$ was incubated with either Ire1$^{cyto}$, or Ire1$^{cyto}$ fused to the constitutive dimerization domain glutathione S-transferase (GST). The reaction mixtures were sampled at the times indicated, analyzed by denaturing polyacrylamide gel electrophoresis and visualized by autoradiography. Cleavage products of the expected sizes were obtained as depicted by the accompanying illustration.
**(C)** ADP potentiates Ire1$^{cyto}$ ribonuclease activity. Ire1$^{cyto}$ was incubated with radiolabelled Xbp1$^{mini}$ in the absence or presence of ADP and the resultant RNA cleavage products were analyzed by denaturing polyacrylamide gel electrophoresis and visualized by autoradiography.
**(D)** ADP is a more potent activator of Ire1 nuclease activity that AMP-PNP. Ire1$^{cyto}$ was incubated with radiolabelled Xbp1$^{mini}$ in the presence of various concentrations of ADP or AMP-PNP. The resultant RNA cleavage products at the 30 minute time point were analyzed by denaturing polyacrylamide gel electrophoresis and visualized by autoradiography.
**(E)** Ire1$^{cyto}$ ribonuclease activity is potentiated by autophosphorylation. Radiolabelled Xbp1$^{mini}$ was incubated with either phosphorylated Ire1$^{cyto}$ or non-phosphorylated Ire1$^{cyto\ (D797A)}$, which lacks protein kinase phosphotransfer activity. The resultant RNA cleavage products were analyzed by denaturing polyacrylamide gel electrophoresis and visualized by autoradiography.
**(F)** Ire1$^{cyto}$ and Ire1$^{cyto\Delta 24}$ cleave Xbp1$^{mini}$ with similar kinetics. Ire1$^{cyto}$ or Ire1$^{cyto\Delta 24}$ were incubated with radiolabelled Xbp1$^{mini}$ in the presence or absence of ADP and sampled at various time points. RNA cleavage products were analyzed by denaturing polyacrylamide gel electrophoresis and visualized by autoradiography.

Supplementary Figure 4

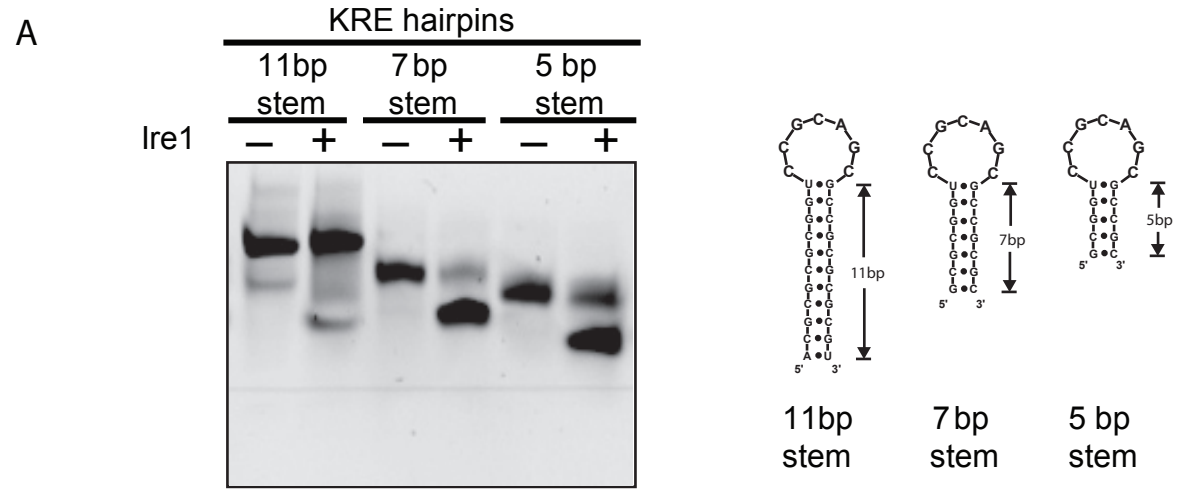


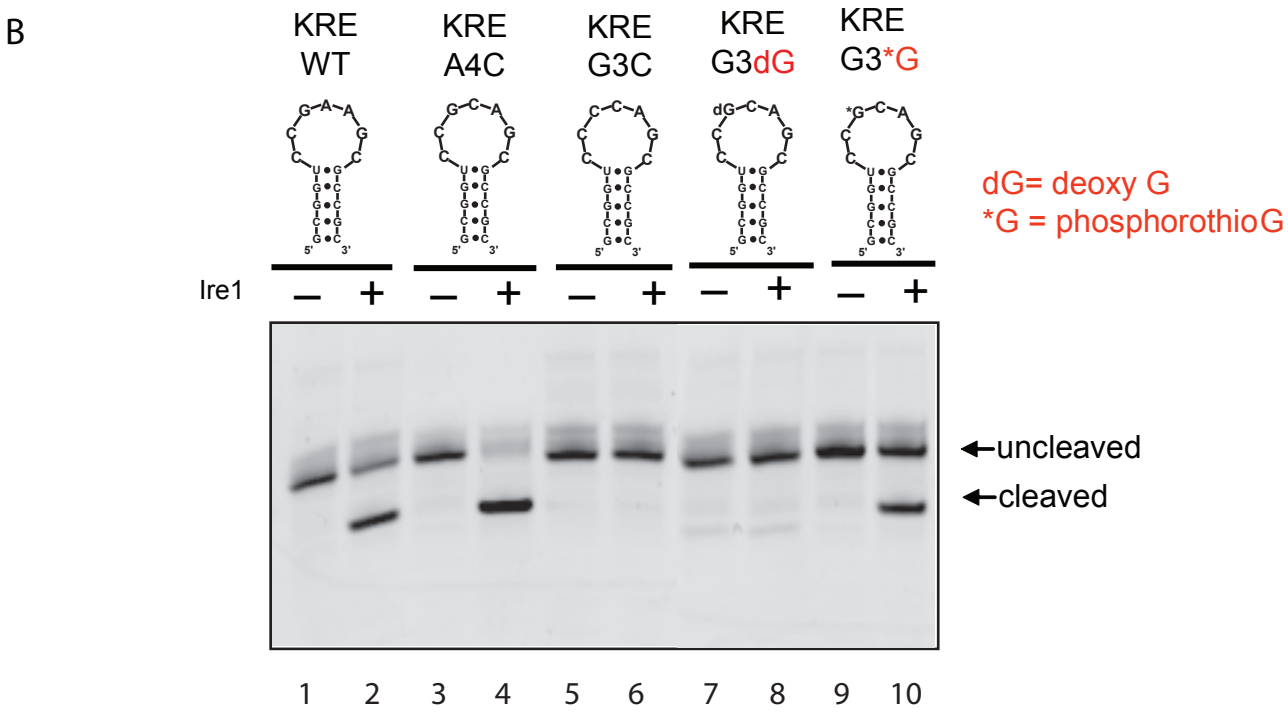

**Figure S4.** Ire1$^{cyto}$ accurately cleaves RNA hairpin substrates at the physiologically relevant positions.
**(A)** Ire1$^{cyto}$ was incubated with 5'-fluorescein-labelled single RNA hairpins of variable stem lengths. Hairpin loop sequences correspond to those of the 3' hairpin of Hac1 mRNA with a A-to-C mutation at the fourth position (denoted A4C). Cleavage products were analyzed by denaturing polyacrylamide gel electrophoresis and visualized by fluorescence imaging. The 5 base-pair stem hairpin was chosen for further analysis (see below).
**(B)** 5'-fluorescein-labelled hairpins with 5 base pair stems containing the indicated substitution or chemical modifications in loop positions were incubated with Ire1$^{cyto}$. The resultant cleavage products were analyzed on a denaturing polyacrylamide gel and visualized by fluorescence imaging. The cleavage profiles indicate that Ire1$^{cyto}$ cleaves the A4C mutant hairpin more robustly than the wild-type 3' Hac1 loop hairpin (compare lanes 2 and 4), as previously reported (Gonzalez, *et. al.*, (1999). EMBO J *18*, 3119-3132), while mutation of the conserved guanosine at the third position to cytosine (denoted G3C) completely abolishes cleavage by Ire1$^{cyto}$ (compare lanes 4 and 6) as previously reported (Gonzalez, *et. al.*, (1999). EMBO J *18*, 3119-3132).Furthermore, substitution of guanosine at position three with deoxyguanosine (denoted G3dG) completely abolished cleavage by Ire1$^{cyto}$, suggesting that the 2'-OH group of G3 may participate in the cleavage mechanism. Demonstrating that Ire1$^{cyto}$ accurately cleaves the 3' Hac1 stemloop at a physiologically relevant position (i.e. after G3) (Gonzalez, *et. al.*, (1999), EMBO J *18*, 3119-3132), introduction of a phosphorothioate substitution of the 3' phosphate group of G3 (denoted G3*G) severely impaired cleavage by Ire1$^{cyto}$.

Supplementary Figure 5

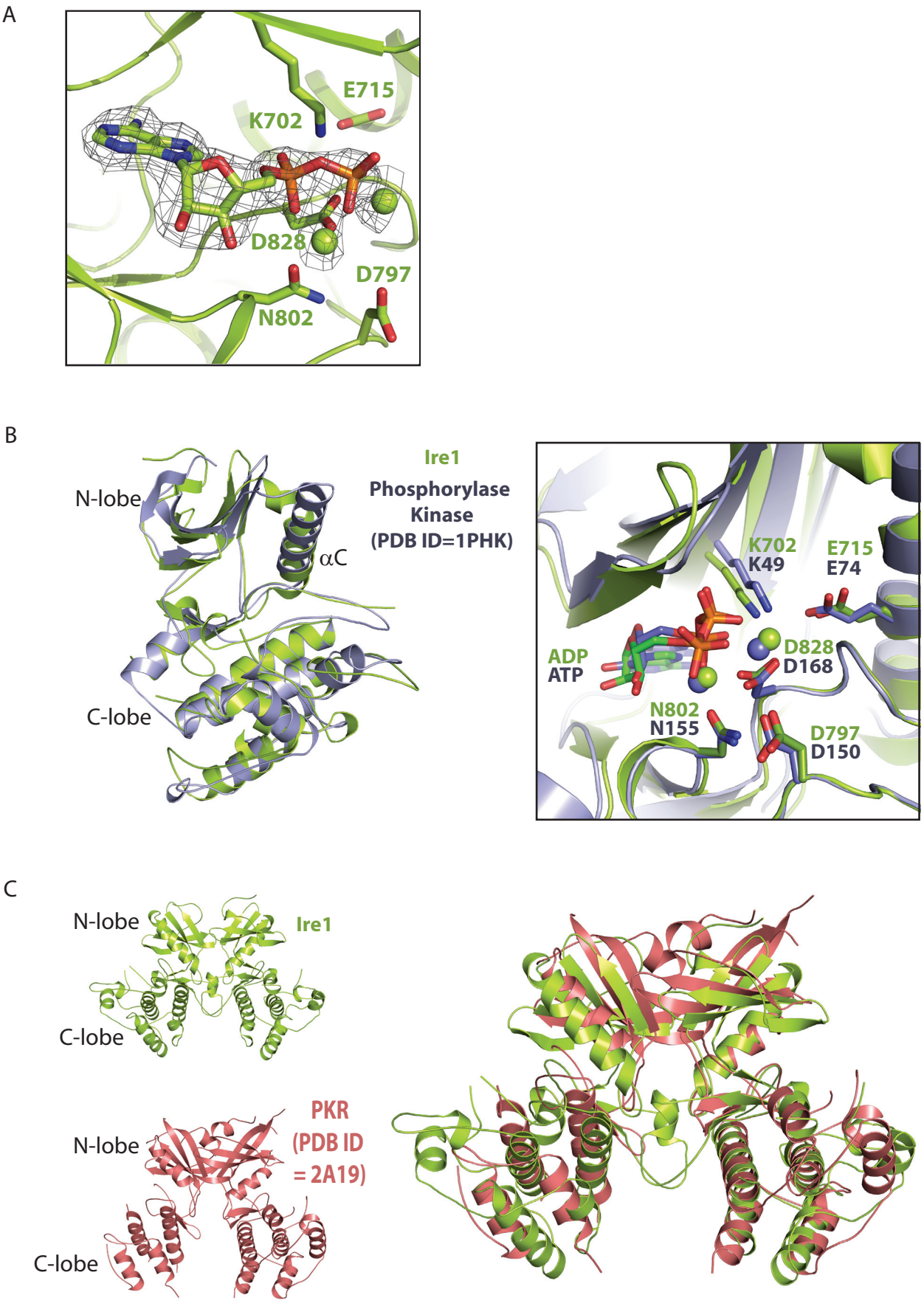

**Figure S5.** Structural features of the protein kinase domain of Ire1
**(A)** Close-up view of the nucleotide binding cleft of Ire1. Key catalytic residues, bound ADP and coordinating metal ions are shown in ball and stick representation. Electron density from the unbiased single anomalous dispersion phased map is show contoured at 3σ.
**(B)** Superposition of the active state kinase domain structures of Ire1 in green and phosphorylase kinase in red (PDB ID=1PHK). Inset displays a zoom in view of the catalytic cleft region highlighting active site residues, bound nucleotide and coordinating metal ions in ball and stick representation. Superposition was performed with SSM (Krissinel, E., and Henrick, K. (2004) Acta Crystallogr D Biol Crystallogr *60*, 2256-2268) (RMSD = 1.66 Å).
**(C)** Comparison of the parallel back-to-back kinase domain dimer configuration of Ire1 in green and the RNA dependent protein kinase PKR (PDB ID = 2A19) in red. Structures in right panel were superimposed using SSM (RMSD=3.72Å ).

Supplementary Figure 6

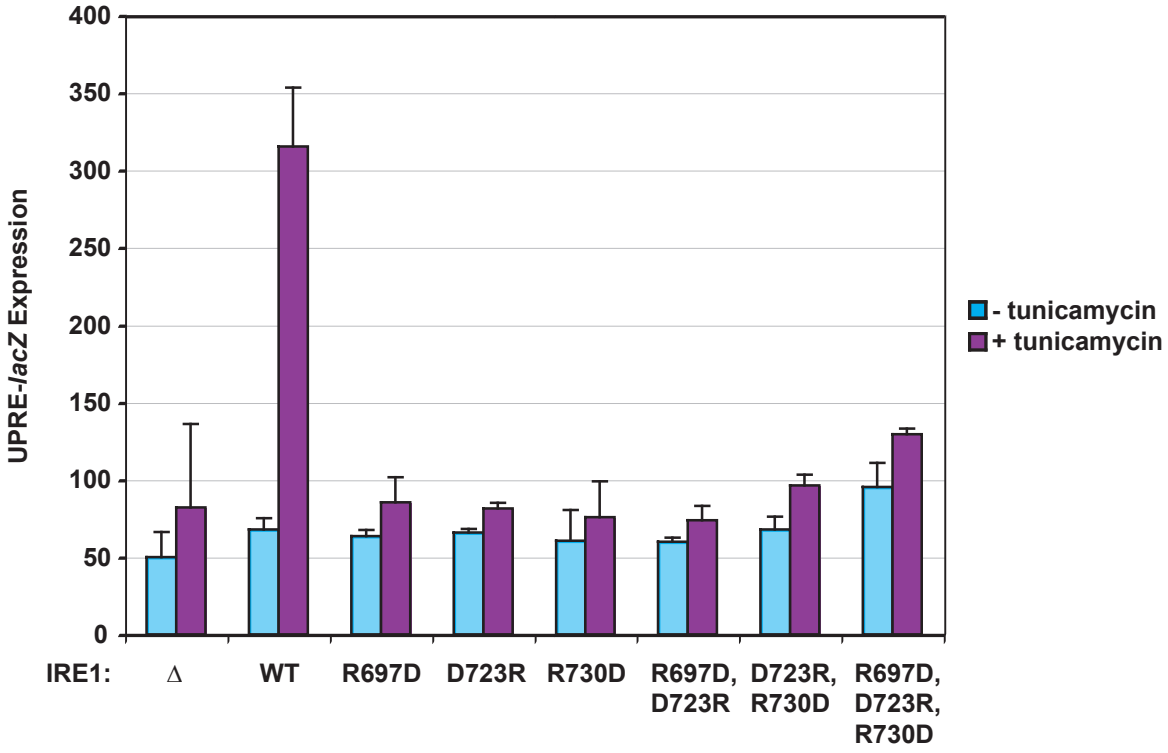

**Figure S6.** Analysis of UPRE-*lacZ* expression
Derivatives of yeast strain F862 (*MAT**a** his3-Δ1 leu2-Δ0 met5-Δ0 ura3-Δ0 ire1::kanMX*) expressing the indicated wild type or dimer-interface mutant FLAG-tagged *IRE1* alleles, or no Ire1 (Δ, vector only control), were transformed with the high copy-number *cyc1-lacZ* reporter plasmid pMCZ-Y (a gift from Drs. Yihong Ye and Will Prinz) containing a single UPR element (UPRE) from the yeast *KAR2* gene. Transformants were grown for 2 hr in SD medium and then transferred to SD medium (-) or SD medium supplemented with 1 μg/ml tunicamycin (+), and harvested after 4 hr growth at 30 ˚C. Cells were harvested and β-galactosidase activities were determined as described previously (Hinnebusch, A. G. (1985) Mol Cell Biol *5*, 2349-2360). Plotted in the histogram are the average and standard error obtained from three independent transformants.

Supplementary Figure 7

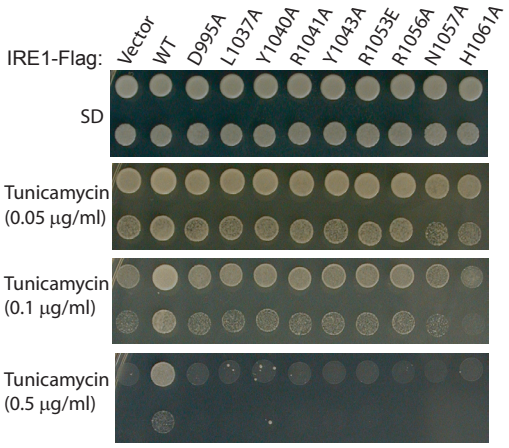

**Figure S7.** Disruption of the putative ribonuclease active site abrogates ribonuclease function in vivo.
*Ire1*-null yeast strains transformed with wild type or the indicated KEN domain single-site mutants of full-length FLAG tagged-Ire1 were spotted on minimal medium supplemented with essential nutrients (SD) or medium containing the indicated concentration of tunicamycin. The negative effect on growth was similar for all mutations throughout the range of concentrations of tunicamycin tested.

Supplementary Figure 8

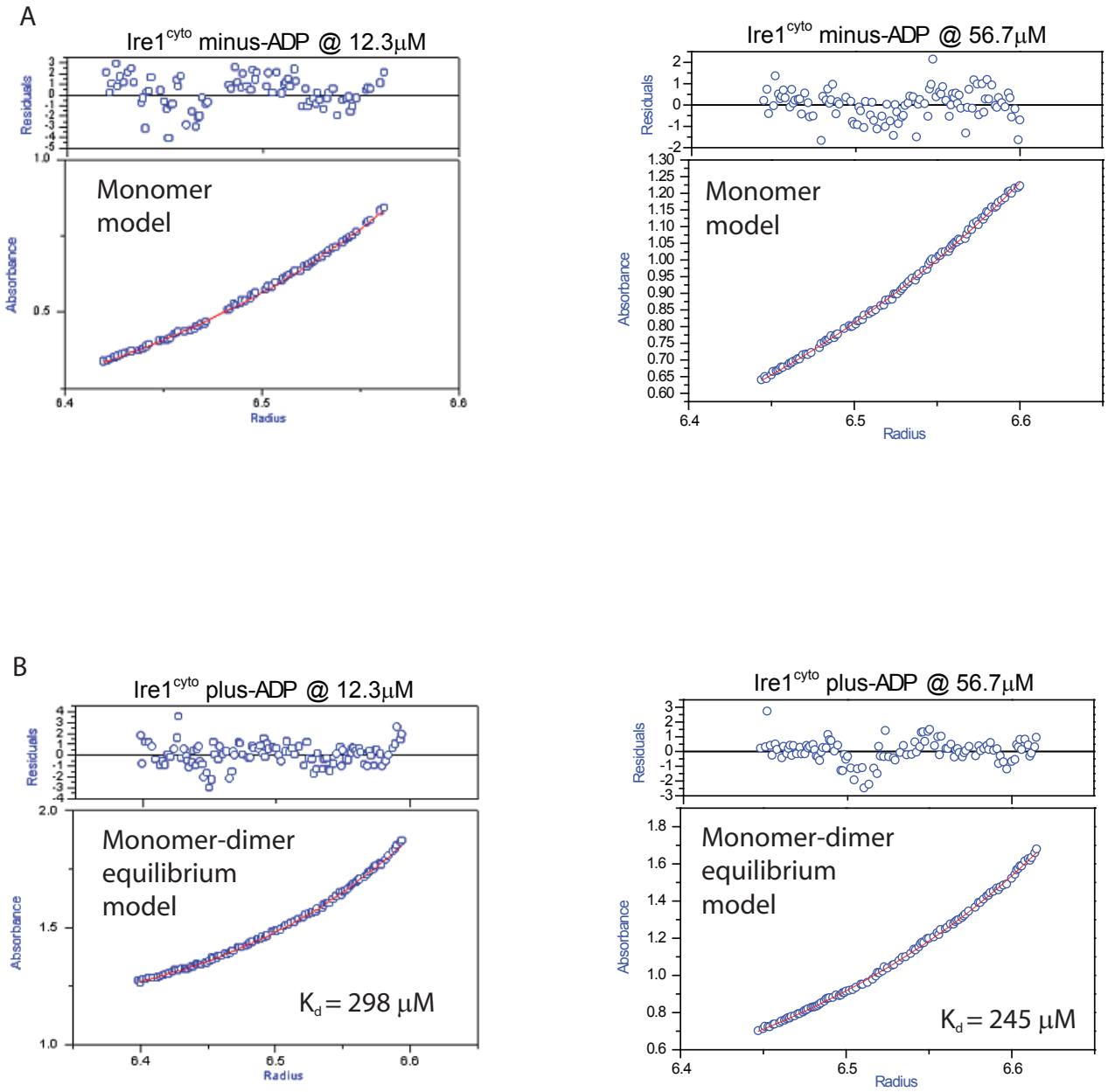

**Figure S8.** ADP promotes the dimerization of $Ire1^{cyto}$
Purified $Ire1^{cyto}$ was subjected to analytical ultracentrifugation analysis in the absence **(A)** or presence **(B)** of 1mM ADP. Each equilibrium sedimentation analysis was performed at three protein concentrations and three speeds. Data shown corresponds to the 12.3μM (data collected at 280nm) and 56.9μM (data collected at 295nm) sample spun at 10,000x G using a Beckman Optima XL-A centrifuge. In the absence of ADP, the data was best approximated by a monomer only model. Fitting data collected in the presence of ADP to a single species model yielded an average molecular weight significantly greater than the theoretical monomer molecular weight (fitted model not shown). The data collected in the presence of ADP was best approximated using a monomer-dimer equilibrium model, which shows a random distribution of residuals, indicative of a good fit (**B**). These results indicate that $Ire1^{cyto}$ exists in equilibrium between monomer and dimer states in the presence of ADP but is exclusively a monomer in the absence of ADP.

Supplementary Figure 9

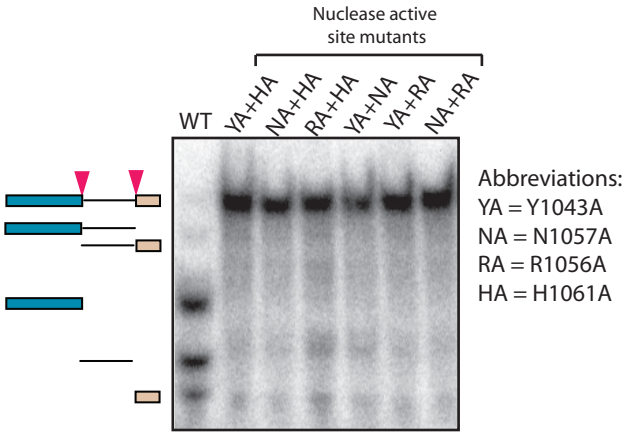

**Figure S9.** The catalytic apparatus of Ire1 for RNA cleavage is formed in *cis*.

All possible binary combinations of mutant $Ire1^{cyto}$ proteins containing nuclease inactivating mutations in the catalytic tetrad within the KEN domain nuclease active site (**Figure 7**) were mixed at equimolar ratios and incubated with radiolabelled $Xbp1^{mini}$. Reactions were sampled at the 30 minute time point and RNA cleavage products were analyzed by denaturing polyacrylamide gel electrophoresis and visualized by autoradiography. No detectable levels of restoration in nuclease activity was observed by mixing different mutants, supporting the notion that the catalytic center in the Ire1 nuclease active site is formed in *cis*.

Supplementary Figure 10

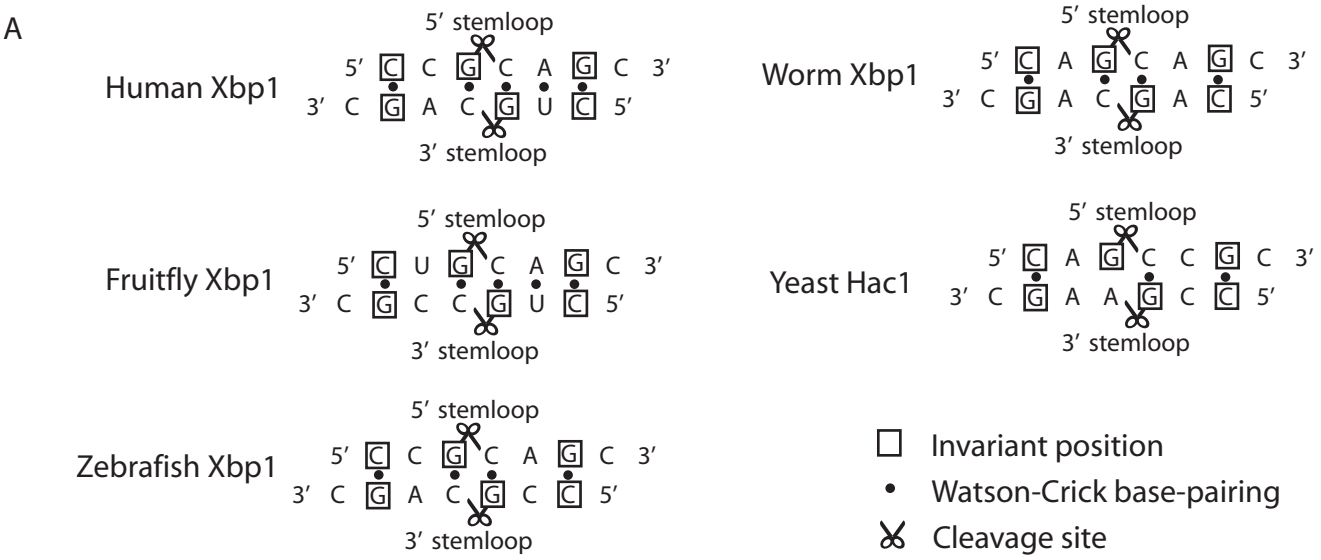


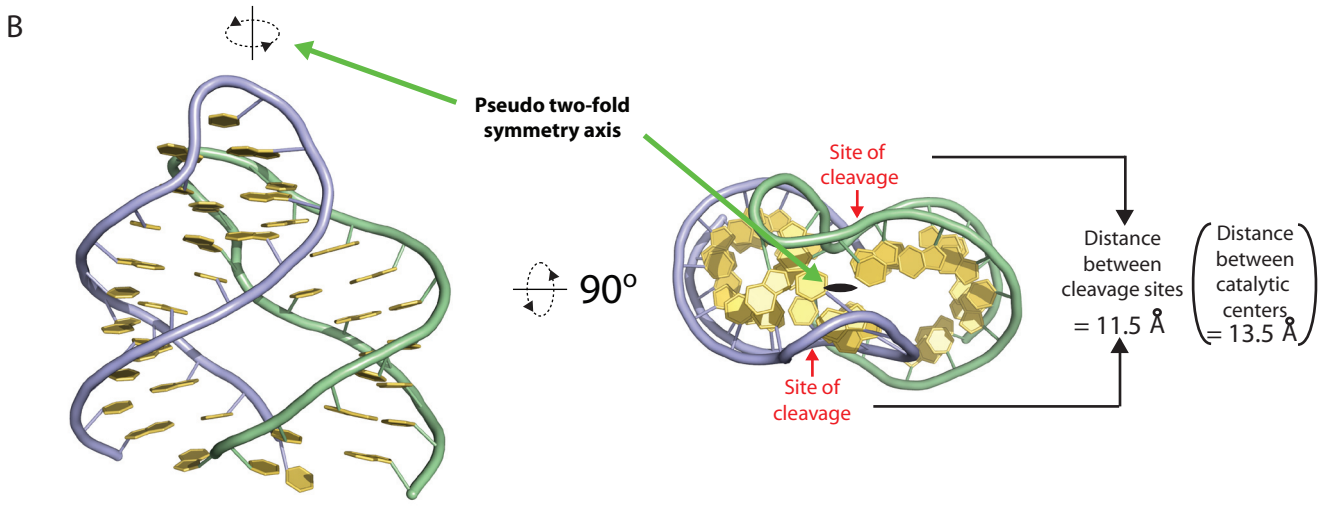


Model of potential kissing hairpin arrangement of Ire1 substrates
(based on PDB ID = 1U8D)

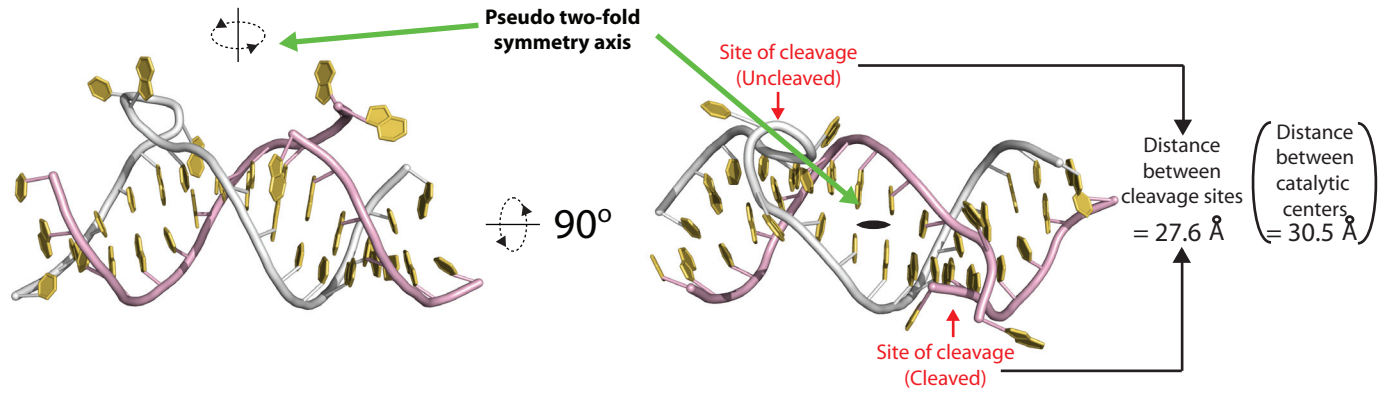


Bulge-helix-bulge motif recognized by tRNA endonuclease
(PDB ID = 2GJW)

**Figure S10.** RNA splicing substrates of Ire1 may form twofold symmetric dimeric structures.
**(A)** Loop sequences in the 5' and 3' hairpin splice junctions of Ire1 target transcripts display a potential for Watson crick base pairing. Loop sequences of paired 5' and 3' hairpin splice junctions of Xbp1 mRNAs from *H. sapiens (human), D. melanogaster (fruitfly), D. rerio (zebrafish),* and *C. elegans (nematode),* and Hac1 mRNA from *S. cerevisiae (yeast)* are shown in a staggered anti-parallel arrangement offset by one nucleotide. Conserved loop positions are demarked by black boxes. Note the pseudo-palindromic nature and extensive Watson-Crick base-pairing between conserved residues in the aligned loop regions.
**(B)** Comparison of the two-fold symmetric nature of a tRNA endonuclease RNA substrate and a proposed kissing hairpin model of an Ire1 RNA substrate.
The proposed tandem kissing hairpin arrangement of an Ire1 RNA substrate is colored blue and green (top).The bulge-helix-bulge (BHB) motif of the tRNA endonuclease RNA substrate is colored in pink and grey (bottom). The locations of the axes of pseudo-two fold symmetry are indicated. The distances between the sites of cleavage in both models correspond closely to the distance between the respective catalytic centers in tRNA endonuclease and Ire1.